Practical Issues for Atom Probe Tomography Analysis of III-Nitride Semiconductor Materials

Fengzai Tang[1], Michael P. Moody[2], Tomas L. Martin[2], Paul A.J. Bagot[2], Menno J. Kappers[1], Rachel A. Oliver[1,*]

[1] Department of Materials Science and Metallurgy, University of Cambridge, 27 Charles Babbage Road,
Cambridge, CB3 0FS, United Kingdom
[2] Departments of Materials, University of Oxford, Parks Road, Oxford, OX1 3PH, United Kingdom

Abstract:

Various practical issues affecting atom probe tomography (APT) analysis of III-nitride semiconductors have been studied as part of an investigation using a *c*-plane InAlN/GaN heterostructure. Specimen preparation was undertaken using a focused ion beam microscope (FIB) with a mono-isotopic Ga source. This enabled the unambiguous observation of implantation damage induced by sample preparation. In the reconstructed InAlN layer Ga implantation was demonstrated for the standard 'clean-up' voltage (5 kV), but this was significantly reduced by using a lower voltage (e.g. 1 kV). The characteristics of APT data from the desorption maps to the mass spectra and measured chemical compositions were examined within the GaN buffer layer underlying the InAlN layer in both pulsed laser and pulsed voltage modes. The measured Ga content increased monotonically with increasing

---

[*] Corresponding author. Tel. + 44 (0)1223 760750. Email address: rao28@cam.ac.uk (R.A. Oliver)

laser pulse energy and voltage pulse fraction within the examined ranges. The best results were obtained at very low laser energy, with the Ga content close to the expected stoichiometric value for GaN and the associated desorption map showing a clear crystallographic pole structure.

Key words: III-nitrides, InAlN, GaN, focused ion beam, Ga implantation, atom probe tomography

INTRODUCTION

III-nitride semiconductors achieve light emission at wavelengths spanning from the ultraviolet to near infrared by exploiting the range of direct band gaps of AlN, GaN and InN and their alloys (Ambacher, 1998; Jarjour, et al., 2007; Nakamura, et al., 1995; Speck & Chichibu, 2009; Zhu, et al., 2013). This leads to wide-ranging current and future applications in optoelectronics, for instance, light emitting diodes (LEDs), laser diodes (LDs) (Zhu, et al., 2013) and single photon sources (Jarjour, et al., 2007). Blue and green LEDs and LDs typically employ ternary quantum well (QW) structures in their active regions which improve their quantum efficiency due to the confinement of carriers (Nakamura, et al., 1995). Internal quantum efficiencies in excess of 70% are routinely achieved for blue-emitting QWs, which is rather surprising given that typical GaN-based devices are grown heteroepitaxially on substrates such as sapphire and silicon, and the resulting lattice mismatch leads to threading dislocation densities in the 10^8 – 10^9 cm^{-2} regime. Even defect densities several orders of magnitude lower would render conventional III-V semiconductor devices inoperable, suggesting that some aspect of the nanoscale structure of nitride QWs makes devices robust to the effects of non-radiative carrier recombination at defect sites (Oliver, et al., 2010). Further development requires precise nanoscale characterisation of these materials. However, in the case of structural analysis by transmission electron microscopy (TEM) (Baloch, et al., 2013; Oliver, et al., 2010; Rhode, et al., 2013; Smeeton, et al., 2003), there is significant concern that the incident high energy electron beam may in fact damage the QWs, hence leading to misinterpretations of the QW structure (Baloch, et al., 2013; Bennett, 2011; Smeeton, et al., 2003). This concern has motivated the increasing application of atom probe tomography (APT) characterisations in nitride research. In addition to avoiding the electron-beam induced damage of TEM, APT has its own unique merits, however characterisation of its limitations and development of optimised experimental protocols specifically for the analysis of III-nitride materials requires further research.

APT is a microscopy technique based on the highly controlled field evaporation of individual atoms from the surface of a very sharp needle-shaped specimen. It is capable of providing three dimensional (3D) microstructural information with near atomic-scale resolution. The chemical identity of evaporated atoms is determined by means of time-of-flight mass spectroscopy (Gault, et al., 2012; Miller, et al., 1996). Until recently, the removal of an atom from the sample in the experiment could only be triggered by the enhanced electric field induced by application of high-voltage (HV) pulse. Hence, APT was conventionally limited to the study of metallic materials, due to their sufficient electrical conductivity. However, contemporary instruments have the capacity to replace the action of the HV-pulse with an ultrafast laser pulse (Kellogg & Tsong, 1980). The advent of pulsed-laser APT has greatly broadened the application of the technique into non-metallic materials, such as metal oxides and nanocomposites (Devaraj, et al., 2013; Kirchhofer, et al., 2013; Tang, et al., 2010). In the case of III-nitrides, Galtrey et al. in 2007 pioneered the application of APT to assess whether indium ‘clusters’ were present in *c*-plane InGaN/GaN multiple quantum wells (MQWs) (Galtrey, et al., 2007). Thereafter, a number of studies have been reported for both polar

(Bennett, et al., 2011; Galtrey, et al., 2008; Gu, et al., 2013; Müller, et al., 2012), semi-polar (Prosa, et al., 2011) and non-polar (Riley, et al., 2014; Tang, et al., 2015) InGaN-based structures, and for AlN-containing materials (Choi, et al., 2012; Mazumder, et al., 2013). All of these studies rely on pulsed-laser APT. When studying GaN nanowires, it has been found that the measured Ga/N ratios deviated from expected stoichiometry at high laser energies (Agrawal, et al., 2011; Diercks, et al., 2013; Riley, et al., 2012; Sanford, et al., 2014). This was attributed to the difference in electric field required to evaporate different elemental species from the material, leading to uncontrolled evaporation and hence preferential loss of nitrogen or nitrogen-containing ions from the experiment. Dawahre et al. in 2013 identified similar limitation. In addition, that study also attempted HV-pulsed APT analysis of a bulk GaN material. In that case, only a mass spectrum was reported, however, it contained a number of unidentified, most likely spurious peaks. A large operational space of experimental conditions remains to be fully explored in the APT analysis of III-nitrides.

The application of APT has also significantly benefited from the development of specimen preparation techniques utilising the dual beam focused ion beam microscope (FIB). Using FIB-based techniques site-specific APT samples can be made from a wide variety of materials. A possible limitation of this approach is potential damage to the specimen by the Ga ion beam. Although it is generally known in the APT community that the damage to the material caused can be limited by lowering the FIB accelerating voltage during the final “clean-up” step, for instance, typical Cu/Co layers and Si materials (Larson, et al., 1999; Thompson, et al., 2006; Thompson, et al., 2007), there is no clear consensus as to the optimal FIB conditions that should be employed for studying III-nitride materials in the ever increasing literature on these materials (Bennett, et al., 2011; Choi, et al., 2012; Dawahre, et al., 2013; Galtrey, et al., 2008; Galtrey, et al., 2007; Gu, et al., 2013; Müller, et al., 2012;

Prosa, et al., 2011). Amidst these, variable ‘clean-up’ FIB voltages, up to 5 kV, have been reported (Bennett, et al., 2011; Gu, et al., 2013). When investigating Ga-containing materials, this issue becomes challenging due to the question of differentiation of FIB-implanted Ga damage from Ga originally present in the sample. Without validation of an effective approach to clean-up, doubt is cast, particularly within the GaN community, on the reliability of APT investigations of Ga-containing materials, for instance, the determination of unintentional alloyed Ga in InAlN layer (Choi, et al., 2014; Kim, et al., 2014; Smith, et al., 2014) and the width of InAlN/GaN interface where the possible existence of small amount of FIB-induced Ga could cast shadow on the results.

In this work, the FIB-induced Ga implantation with different ‘clean-up’ voltages was experimentally evaluated using an InAlN layer grown on a *c*-plane GaN pseudo-substrate. InAlN/GaN structures are relevant to, for example, fabrication of high electron mobility transistors (Dawahre, et al., 2013). The motivation for using InAlN rather than GaN in our experiment was to facilitate the observation of Ga from FIB implantation. An approach was also established to effectively differentiate the FIB-induced Ga from sample-contained Ga based on the fact that a monoisotope Ga source was employed in FIB. The analysis has revealed some unintentional incorporation of Ga into the InAlN layer during the growth process, the origin of which has been discussed in some recent reports (Choi, et al., 2014; Dawahre, et al., 2013; Kim, et al., 2014; Smith, et al., 2014; Zhu, et al., 2012). Since GaN forms the basis of a wide range of optoelectronic and electronic devices, the impact of APT experimental conditions on analysis of the GaN pseudo-substrate in both pulsed laser and pulsed voltage modes was explored. This work aims to provide guidance on the practical issues which must be overcome for accurate analysis of III-nitrides by APT.

MATERIALS AND METHODS

MATERIALS

The InAlN/GaN sample was grown on a pseudo-substrate by metal-organic vapour phase epitaxy using a Thomas Swan 6 × 2” close-coupled showerhead reactor. The pseudo-substrate consisted of ~ 6 µm of GaN grown on *c*-plane sapphire using the method described by Datta et al. (Datta, et al., 2004). Prior to the InAlN growth, a ~ 500 nm thick buffer layer of GaN was grown on the pseudo-substrate. InAlN was then grown at 790°C under a nitrogen carrier gas using ammonia, trimethylindium (TMI) and trimethylaluminium (TMA) as precursors. The optimised growth conditions identified by Sadler et al. in 2011 were employed (Sadler, et al., 2011). Basic sample characterisation was carried out using XRD, employing a Philips/Panalytical PW3050/65 X'Pert PRO high resolution horizontal diffractometer, and details of the method may be found in Sadler et al. in 2011. The results of these preliminary investigations suggested an InAlN layer thickness of 90 ± 10 nm and a composition of (18 ± 2) site%, close to lattice matching. It should be noted that these values assume no incorporation of Ga into the InAlN layer.

METHODS

APT sample preparation using a FIB-based in situ lift-out method

APT samples were prepared using a dual beam FIB (FEI Helios NanoLab™) in which a Kleindiek micromanipulator was configured inside the chamber for *in-situ* lift-out (Larson, et al., 1999; Thompson, et al., 2007). In order to systematically evaluate FIB implantation caused by sample preparation, the following procedures were adopted:

(i) An InAlN/GaN sample was first coated with a ~50 nm thick Pt layer using a sputter coater before loading into the FIB chamber;

(ii) A strip of Pt with dimensions of about 20 µm (length) × 2 µm (width) × 1 µm (thickness) µm was further deposited on the sample surface using electron beam (e-beam) assisted Pt deposition at voltages of 5-10 kV with beam currents of 1.4-2.7 nA. This approach was used to avoid possible Ga implantation into the sample surface, which could occur during the FIB-induced Pt deposition (Cullen & Smith, 2008; Thompson, et al., 2007);

(iii) Following the standard protocols (Thompson, et al., 2006; Thompson, et al., 2007), hereafter, trench-cutting, extraction and mounting of the sample wedge were performed at 30 kV (FIB) with variable beam currents 9.3 nA to 24 pA, and from this sample wedge a number of sections were mounted onto the Si posts of a standard flat-top microtip array coupon;

(iv) The samples were then sharpened using variable beam currents (0.44-0.13 nA) at a 15 kV FIB voltage, making sure to retain at least ~80 nm of the Pt layer.

(v) The final FIB 'clean-up' procedure was carried out at different voltages (5, 3.5 and 1 kV) on each individual sample. During this step the FIB processing was closely monitored via simultaneously SEM imaging, and the milling was stopped at as close to the Pt/InAlN interface as possible. Post APT examination of the very first evaporated ions in the data sets showed no apparent Pt peak in the mass spectrum in the case of 3.5 kV clean up, but a very small number of Pt counts in the cases of 1 kV and 5 kV. Thus, these Pt counts were ignored in the later APT analysis of Ga-implantation.

APT analysis

APT experiments were carried out using a reflectron-fitted Cameca LEAP 3000X. The system can be operated in either pulsed-laser mode or HV-pulsing mode. The laser position was aligned onto the apex of the APT sample by maximising the detection rate. The laser had a wavelength of 532 nm with a nominal pulse duration of 12 ps and a spot size of ~ 10 µm.

The base temperature of the sample was set at 30 K, and a constant pulse repetition rate of 200 kHz was used for both modes. 3D reconstruction was performed using the IVAS^{TM} software package (CAMECA Version 3.6.6). To assist the reconstruction, SEM (scanning electron microscope: FEI Helios NanoLab™) images were also taken from some specimens before and/or after APT analysis (Prosa, et al., 2013).

A pulsed laser mode was used to analyse the InAlN/GaN layer for the examination of the FIB-implanted Ga content. The average detection rate was set at 0.005-0.01 average ions per pulse. A laser pulse energy of 0.5 nJ was employed for analysis of the InAlN layer. In most cases the laser energy was gradually reduced when the analysis reached the underlying GaN to retain an appropriate stoichiometry. APT samples prepared with 'clean-up' voltages of 5, 3.5 and 1 kV were examined.

Both laser-pulsed and HV-pulsed analysis were carried out on the underlying *c*-plane GaN buffer layer after the analysis of InAlN layer. The impact of laser pulse energy was examined across a wide range of values from 0.004 to1.0 nJ from a single APT specimen. About 10^6 detector hits were collected at each energy at a constant detection rate of 0.01 average ions per pulse. The datasets were acquired in order of increasing laser energy, 0.004, 0.008, 0.015, 0.1, 0.3, 0.5, 1.0 nJ. This was followed by a repeat of the 0.3 nJ condition so as to estimate the uncertainty caused due to the evolution of specimen geometry.

The effect of pulse fraction (PF) on HV pulsing mode was also explored. For these experiments the detection rate was held constant at an average of 0.01 ions per pulse on the same tip, and ~ 10^6 detector hits were collected at each pulse fraction: 30%, 20%, 40%, 25% and 20% again for a repeated run. After completion of these, a data set of 10^6 ions at laser pulse mode was also acquired at 0.065 nJ in order to get a direct comparison between the two modes.

RESULTS

Ga implantation induced by FIB sample preparation

Natural Ga is composed of two isotopes, i.e. the 69 Da peak (Ga-69) with a natural abundance of 60.1% and the 71 Da peak (Ga-71) with 39.9% abundance (Miller, et al., 1996). The trimethyl gallium used for GaN growth is expected to exhibit this isotopic ratio. However, the ion source in the FIB instrument contains monoisotopic Ga-69. The reconstructed spatial distribution of all Ga atoms detected in the APT specimen made with a 5 kV 'clean-up' voltage is depicted in Fig. 1; this includes Ga atoms implanted in the FIB and those from the original growth of the sample. Fig. 1(a) is a 3D reconstruction, for clarity showing only 20% of the detected Ga atoms (royal blue). A 1 at.% In isosurface is used to mark the InAlN/GaN interface. The z-axis marked in the figure represents the APT reconstruction axis along the specimen tip, although the reconstructed image shown is slightly tilted for a better visualization. This direction is almost perpendicular to the InAlN/GaN interface and approximately parallel to the direction of incidence of the ion beam during the annular milling and final cleaning steps, and hence is at approximately 180° to the growth direction. Ga atoms are visible in the nominally InAlN layer both close to the tip apex and close to the InAlN/GaN interface. A close-up of the apex of the specimen in Fig 1(a), is shown in more detail Fig. 1(b), where for the sake of clarity only 50% of the detected Ga atoms (royal blue, large size dots) and 50% of the detected Al atoms (light blue, small size dots) are shown. Further, Fig. 1(c) represents a 5 nm thin slice extracted from (b) as indicated by the rectangular box in Fig. 1(b). These reconstructions show significant levels of implanted Ga towards the exposed top sample surfaces.

A 1D concentration profile for the Ga-69 content along the z-axis of the reconstruction in Fig. 1 is presented in Fig. 2(a). This figure also includes corresponding data from the other samples prepared using different ‘clean-up’ voltages. The z-coordinates of the three data sets are aligned so that the InAlN/GaN interface is in the same position for each voltage. Close to the apex of the tip (i.e. close to the minimum z in each case), a significant concentration of monoisotopic Ga is seen for the samples prepared using 5 kV 'clean-up' voltage, but this appears reduced at lower voltages. The measured Ga consists of about 95% Ga-69 Da, suggesting a concentration of ~ 10 at.% for the FIB-implanted Ga. Measurable implantation extends to a depth of ~ 20 nm for the case of 5 kV, whereas for the samples finished at 3.5 kV and 1 kV, implantation of Ga-69 was far less obvious, if present at all within the errors.

The unintentional incorporation of Ga during InAlN growth is also observed. Fig. 2(b) shows a proximity histogram (proxigram) which plots the In, Ga and Al concentration as a function of distance across the InAlN interface for the 5 kV-cleaned sample. Ga concentration amounts to about 20 site% from the InAlN/GaN interface, and the Ga-69 profile indicates that FIB implanted Ga is at a negligible level, suggesting that it originates from sample growth. This proxigram reveals a relatively sharp transition from GaN to InAlN, and the width of the interface is only ~ 1-2 nm when measured from 90% of average values of the plateau regions in the InAlN layer to essentially zero in the GaN layer for both In and Al profiles. However, in every case a long Ga tail is observed penetrating into the layer which had been assumed to be pure InAlN with an amount of less than 1 at.%. The unexpected incorporation of Ga into InAlN, in the absence of any Ga flux, was previously attributed to the residual Ga-containing materials in the growth environment (Choi, et al., 2014; Kim, et al., 2014; Smith, et al., 2014) and the possible inter-diffusion from the underlying GaN layer

(Dawahre, et al., 2013; Zhu, et al., 2012). Our XRD analysis of the In content of this layer assumed that the InAlN layer did not contain any Ga. It is interesting to note that despite this source of error, in the APT data at the distance of 60 nm region away from the InAlN/GaN interface in Fig. 2(b) the measured In content is approximately 20 site%, in reasonable agreement with the XRD value.

APT analysis of *c*-plane GaN in laser-pulse mode

Fig. 3 shows desorption maps of the GaN buffer layer collected at different pulse laser energies for the cases of 0.004 nJ, 0.1 nJ and 0.5 nJ; each data set contains about 10^6 ions. The desorption map is the 2D histogram of collected ion-hits across the surface of the position sensitive APT detector. Areas with a low density of hits are shaded purple and blue, and high density areas are shaded orange and red. A crystallographic pole structure with distinct 6-fold symmetry is clearly revealed in the case of 0.004 nJ experiment (Fig. 3(a)), corresponding to a {0001} plane projection. With increasing laser energy the pole structures gradually become more blurred.

The mass spectra obtained at different laser energies are presented in Fig. 4. Fig. 4(a) is an overview of mass spectrum at 0.004 nJ, and Figs. 4(b) and 4(c) highlights a region of interest within the mass spectra compared across selected laser energies. In Fig. 4(a), the identified nitrogen and gallium ionic species detected in the APT experiment are N_2^+, N^+, and N^{2+} ions, and Ga^+, Ga^{2+}, and Ga^{3+} respectively, and the complex molecular ions of N_3^+, GaN^{2+} and GaN_3^{2+} are also present. The contribution of N_2^{2+} at 14 Da may be treated as negligible, because no significant 14.5 Da peak was observed, in agreement with previous reports (Agrawal, et al., 2011; Dawahre, et al., 2013). Complex-molecular ions are seen at high laser energy conditions, whereas the high charge state Ga^{3+} ions appear at low laser energy as depicted in Fig. 4(b). The main peaks of N_2^+, Ga^{2+} and Ga^+ ions also varied considerably with increasing pulse laser energy, as depicted in Fig. 4(c). In the case of 0.004 nJ the dominant peak in the mass spectrum is N_2^+ at 28 Da, but it shifts to Ga^+ at 69 Da at 0.3 nJ and over. The mass spectra in Figs. 4(b) and 4(c) were normalized relative to the Ga^{2+} peak (34.5 Da) to facilitate comparison. A small number of GaN_2^{2+} ions appears only at a relatively high laser energies, which might be related to the stability of these molecular ions at certain field strengths (Tsong, 1984).

A quantitative analysis of the mass spectra at different laser energies is illustrated in Fig. 5. In Fig. 5(a), the charge-state-ratio of Ga^+/Ga^{2+} ions increases over 100 times as the laser energy increased from 0.004 nJ to 1.0 nJ. This clearly indicates the effect of the reduced electric field that is required as a result of the increase in laser pulse energy. The measured ratios of molecular species of GaN_3^{2+} over all detected ions increases with increasing laser energy up to 0.1 nJ, and then decreases (Fig. 5(b)). The reason for this reduction remains unclear, but it is presumably related to irregular evaporation at high laser energies. The percentage of the total number of detector hits that were multiple hit events (Fig. 5(c)) decreased with increasing laser energy from about 22% at 0.004 nJ to 4% at 1 nJ. Fig. 5(d) shows the variation with laser energy of the ranged ion ratio which can be considered an approximate measure of the signal-to-noise ratio. It was calculated by taking the ratio of the total number of ranged ion counts (i.e. detector hits identified as actual ions from the specimen and incorporated into the reconstruction) to the total number of all counts (ranged and unranged) across the entire mass spectrum from 0 to 120 Da. This suggests that the signal to noise ratio is best at relatively low pulse laser energy, i.e., less than 0.1 nJ, but deteriorates at higher energies. Fig. 5(e) shows the influence of laser energy on Ga content which changed gradually with increasing laser energy. The GaN layer is expected to exhibit a 1:1

stoichiometric composition. The Ga content approached the expected value of 50% only at the lowest pulse laser energy (~ 55% at 0.004 nJ), whereas the most severe deviations are observed at high energy (~ 95% at 1.0 nJ).

The effective pulse fraction for laser energy was also calculated using a similar approach to that used in reference (Gault, et al., 2010). The representative standing voltage was estimated from the voltage curve obtained at each laser energy. It was then plotted against the corresponding laser energy, from which a reference voltage (here, 9650 V) at zero laser energy was estimated by graphically extrapolating the tendency of the curve. It should be noted that the plot was not suitable for a linear fit. The estimated effective pulse fraction was below ~ 5% for laser energies less than 0.015 nJ, and ~ 14% at 0.1 nJ and ~ 30% at 1.0 nJ

APT analysis of *c*-plane GaN in HV-pulse mode

APT analysis of GaN buffer layer in HV pulsing mode for different pulse fractions (PFs) is shown in Fig. 6. Fig. 6(a) depicts a desorption map acquired at a 20% PF, showing crystallographic pole structures. Increasing the pulse fraction from 20% to 40% led to a slight degradation of the pole structures in terms of the 2D visualisation. Additional significant erroneous peaks were also observe after each large peak such as N^+, N_2^+, Ga^{2+} and Ga^+ ions (as designated in Fig. 6(b) by the arrows and labeled in Fig. 6(c)), the mechanism behind which is not clear. As such, the identification of peaks in the mass spectrum is much more complicated in voltage mode and presents significant difficulty in obtaining appropriate compositions.

The mass spectrum obtained at the 20% PF is illustrated in Fig. 6(b). Similar to the mass spectrum obtained at the 0.004 nJ in Fig. 4(a), the dominant detected ionic species are N_2^+

and N^+ ions for N, and Ga^+, Ga^{2+} for Ga. The higher charge state ion of N^{2+} and Ga^{3+} ions and the molecular species N_3^+, GaN^{2+}, and GaN_3^{2+} were also observed. The striking feature in the mass spectrum is the presence of broad peaks associated with the larger peaks, as indicated by the arrows. The origins of these broad peaks are unclear, since it is apparent that they are not representative of a time-of-flight of an ion from the specimen to the detector. Fig. 6(c) shows the Ga^+ and Ga^{2+} peaks at the different pulse fractions, where the counts were normalized with respect to the 34.5 Da peak associated with the Ga^{2+} ions for comparison. The relative position of the two broad peaks associated with Ga^+ and Ga^{2+} was approximate 2 Da and 1 Da respectively, as depicted in the figure.

The voltage PF also showed a considerable impact on the measurement of the Ga content (Fig. 6(d)). Although about 50 at.% Ga was measured at the 20% PF, it shifted markedly, to 75 at.%, at the 40% PF. After the identification of normal peaks in the mass spectrum, the broad peaks following the known large peaks such as N^+, N_2^+, Ga^{2+} and Ga^+ ions were assigned in the regions where they have prevalently large counts over the adjacent backgrounds. For example, the broad peak associated with N_2^+ (28 Da) was ranged as ~ 29.1-29.7 Da in the case of 40% PF. The broad peaks in the mass spectrum induced an uncertainty, of up to 5 at.%, on the measured Ga composition. It should be noted that the analysis of broad peaks is difficult, and here is merely to provide a crude estimation in terms of their influences on the quality of mass spectrum and measured composition. The ranged ion ratio over entire mass spectrum (0-120 Da) was about 80% without taking the broad peaks into account. In addition, the percent of multiple hits decreased from 18% at 20% PF to 7% at 40% PF.

DISCUSSION

Evaluation of FIB-induced Ga damage and unintentional Ga incorporation during growth

To ensure that the implanted Ga retained in the APT reconstruction resulted from the 'clean-up' stage of the sample preparation, the FIB-induced damage during the sample shaping prior to clean up was minimised by using a 15 kV FIB voltage for shaping, instead of the more usual 30 kV. In addition, a thick Pt layer (i.e. thicker than ~ 80 nm) was retained before starting the 'clean-up' procedure, again to try and prevent Ga implantation into the InAlN during the sample shaping stage. Previously, Thompson et al. in 2007 ((Thompson, et al., 2007)) estimated the stopping range of Ga ions in Pt using SRIM, and it was found that a Pt layer with a 10 nm thickness was necessary in order to avoid Ga implantation at 30 kV, and Cullen et al. ((Cullen & Smith, 2008)) found that the region affected by FIB can be up to 32 nm at 30 kV in an AlGaN-based structure. It should be noted that the work by Cullen et al. was based on the TEM examination, whereas the effects of Ga-implantation damage in this work has been directly characterized from an APT reconstruction.

The original intention of this study was to use InAlN as a Ga-free nitride material to assess FIB damage in this family of materials. However, it ultimately proved necessary to use the isotopic purity of the FIB implanted Ga to differentiate it from Ga unintentionally incorporated during crystal growth. FIB-induced Ga was clearly identified within the samples prepared with relative high 'clean-up' voltages of 5 kV (Figs. 1 and 2), suggesting that a low 'clean-up' voltage, below 5 kV, is necessary to minimize FIB-induced artefacts at the top of the reconstructed volume. However, the amount of Ga implantation in the first few nm of the reconstructed volume (i.e. the minimum z value in each curve in Fig. 2(a)) does not increase monotonically with increasing 'clean-up' voltage. This measurement may in part be influenced by the fact that some material at the very apex of the tip at the start of the APT experiment could not be correctly collected and/or reconstructed. It is known that generally at the apex for a newly prepared tip some material needs to be field evaporated before a stable tip end-form may be formed. This process is likely to involve irregular field evaporation and may lead to loss of the material that contained FIB-implanted Ga to a large extent (Thompson, et al., 2007). Moreover, before APT data acquisition starts, the sample has to be precisely aligned relative to the local electrode. The effects of these will probably be limited, however, it will not be consistent between samples and hence it is not possible to extract precise Ga implantation depths from the APT reconstructions.

It should be noted that the FIB-induced Ga implantation was examined in an InAlN layer, and Ga implantation in the FIB is closely related to sample properties, such as bond strength, ion channelling effects (Kempshall, et al., 2001) and grain boundaries (Tang, et al., 2012). For instance, it has been found that ion channelling effects may cause a reduced sputtering yield, but an expected deeper penetration depth into materials in the FIB study of Cu grains (Kempshall, et al., 2001). In terms of binary III-nitrides, the metal–N bond length in the wurtzite structure increases from AlN, to GaN and to InN (Ambacher, 1998), being associated with corresponding bond energy of 2.88 eV, 2.2 eV and 1.93 eV respectively (Keller & DenBaars, 2003). It thus would be expected that the damage in GaN and InN would be relative larger over that of AlN in identically operational conditions. Additionally, this work can also provide some insight on the FIB-based TEM specimen preparation of III-nitride materials.

Desorption map, mass spectrum and measured composition

The *c*-plane GaN buffer layer was examined as a function of pulse laser energy and voltage pulse fraction (PF) respectively, and the characteristics of the desorption map, mass spectrum, and measured composition are discussed in this section, with comparisons being drawn between the two modes.

(i) Desorption map

The gradual degradation of the pole structures in the desorption maps (Fig. 3) with increasing laser energy implies the occurrence of a less controlled sequence of field evaporation as the surface ions are supplied with an increasing amount of thermal energy. It is known that this thermal energy supplied by laser illumination can also induce surface migration on the tip surface, introducing ion trajectory aberrations detrimental to reconstruction analysis (Gault, et al., 2010). Hence, the visibility of crystallographic pole structures in desorption maps may be used as an indirect reference for the quality of lateral resolution in 3D reconstructions. The clearest pole structures were observed in HV-pulsing mode for the case of 20% PF (Fig. 6(a)), being comparable to that obtained at low laser energy of 0.004 nJ (Fig. 3(a)), or perhaps even slightly sharper. With increasing PF, the pole structures on desorption maps showed a slight change in terms of the 2D visualization, although the detected Ga composition (discussed as below) deviated considerably.

(ii) Mass spectrum

The major peaks in mass spectra obtained at relative high laser energy (e.g. larger than 0.1 nJ) were associated with ‘thermal tails’ (Kirchhofer, et al., 2013). At higher laser energies the specimen must dissipate an increasing amount of heat between pulses. Thermal tails occur because, depending on the rate of this heat dissipation, for a time after the application of the pulse there is a probability that surface atoms will maintain enough thermal energy to be field evaporated. If this evaporation occurs long enough after the pulse, meaningful time-of-flight information is lost and then the ion is simply registered as noise in the mass spectrum. Thus, the reduction of the ratio of ranged ion counts (Fig. 5(d)) at high pulse laser energies is related to the occurrence of these 'thermal tails' and uncorrelated field evaporation between pulses while heat is dissipated.

The observed ion species in the mass spectrum in laser mode (Fig. 4(a)) are consistent with previous reports on the analysis of various GaN-based semiconductors (Agrawal, et al., 2011; Bennett, 2011; Dawahre, et al., 2013; Riley, et al., 2012; Sanford, et al., 2014). The relatively large portion of multiple hit events at low laser energy (Fig. 5(c)) could be pertinent to the dissociation mechanism proposed by Stepien et al. (Stepień & Tsong, 1998), since the dissociation of a single complex molecular ion into two or more fragment ions after each laser pulse (or voltage pulse (Yao, et al., 2010)) would lead to a multiple-hit event. Further, since the probability of the dissociation process would tend to be larger at a relatively more intense electric field, an increased fraction of multiple hits would be expected at a low laser energy. This is in line with the decrease of molecular species observed in the low laser energy regime in Fig. 4 (b). It should be noted that the fraction of multi-hits (e.g. ~ 22% at 0.004 nJ) is not very high in contrast to other non-metallic materials for instance, TiSiN, where it can amount to over 50% (Tang, et al., 2010).

For the mass spectra obtained at different PFs: broad peaks appeared after each large peak (Figs. 6(b) and (c)). These broad peaks are associated with a longer recorded flight time than that of the relevant main peak. Similarly, in the analysis of GaN materials, Dawahre et al. in 2013 found a number of as yet unidentified peaks, particularly in the range of 80-95 Da. When analyzing AlMgSi, Gault et al. in 2012 observed a number of minor peaks in the mass spectrum, which they term 'replicas'. It was suggested that the minor peaks may arise from the delayed evaporation induced by a reflected voltage pulse. While the peaks observed in this study are more extreme, they could be interpreted in the context of the mechanism proposed by Gault et al.. Overall, interpretation of this phenomena closely depends on the field evaporation mechanisms of wide band gap semiconductors and insulators which are not well established (Kelly, et al., 2014; Sanford, et al., 2014; Silaeva, et al., 2013; Tamura, et al., 2012).

The broad peaks in the mass spectrum may account for over 10% of total counts. Without including these peaks, the ratio of ranged ions over entire mass spectrum is about 80%, less than those obtained in the cases with low pulse laser energies below 0.1 nJ (Fig. 5(d)). This was further confirmed by the laser-pulsed run completed immediately after the final voltage-pulsed run on the same tip at 0.065 nJ pulse laser energy, in which a ratio of about 90% was observed. Ignoring the contributions from the broad peaks observed in pulsed voltage mode, the mass spectra which show close to the expected GaN stoichiometry (i.e., 20% PF (Fig. 6(b)) and 0.004 nJ (Fig. 4(a))) have similar characteristics in both pulsing modes. Specifically, the N_2^+ ions are the most intense peak for nitrogen species, and the Ga^+ ions for gallium species, consistent with previous reports for pulsed laser (Agrawal, et al., 2011; Dawahre, et al., 2013; Riley, et al., 2012) and pulsed voltage (Dawahre, et al., 2013) modes.

One of main reasons for the failure of an APT analysis is premature fracture of the sample, which is induced by electrostatic stress (Moy, et al., 2011) imposed on the APT tip. When analysing non-metallic materials, the sample may suffer a high stress level due to the large voltage attenuation resulting from insufficient conductivity (Melmed, et al., 1981). The electrical resistivity of GaN may be considerably influenced by the growth condition (e.g. growth rate and thickness), the level of unintentionally doped impurity (Götz, et al., 1999) and crystal imperfection. For instance, a wide range of 10^{-2}-1 Ω cm was reported at 100-10 K

(Ilegems & Montgomery, 1973). Pulsed laser mode is therefore often used in preference to pulsed voltage mode, because the increased temperature of the APT sample upon laser illumination may reduce the field strength required for field evaporation, and thus alleviate field-induced stress on the sample. In this work, however, the analysis with low laser energy (less than 0.015 nJ) yielded an effective pulse fraction < 5%, which means that there is no significant mitigation of the standing voltage. However, the APT sample in laser-pulse mode does not suffer from the cyclic stresses occurring in voltage mode (Gault, et al., 2012) which may be an advantage to avoiding fracture.

In addition, the mass resolving power (Gault, et al., 2012; Kelly, et al., 2014) of the main peak at 69 Da in each mass spectrum obtained in HV mode was in the range of ~ 750-1030 at full-width at half-maximum (FWHM), which was less than those obtained in pulsed laser mode (the range of ~ 1190-1260). This was further confirmed by a run in pulsed laser mode which was included after a series of voltage runs on the same APT tip. It should be noted that the influence of tip geometry on the mass resolving power (Tang, et al., 2010) has not been excluded in above estimations. In fact, the improved mass resolving power in pulsed laser mode is generally expected, because energy deficits occurring in HV pulsing can induce a spread in the time-of-flight of the ions, limiting mass resolving power (Müller & Krishnaswamy, 1974). The broad peaks could have a detrimental influence on APT analysis in voltage mode (as discussed above). This effect can lead to the difficulty in accurately assigning mass spectrum peaks: for example, in the case of 30% PF where the broad peak overlaps with the relevant Ga^+ peak (Fig. 6(c)). Thus, HV pulsing mode was not a viable option for the analysis of GaN semiconductors in this work.

(iii) Measured chemical composition of c-plane GaN

The measured Ga composition increased monotonically with increasing pulse laser energy and voltage pulse fraction within the experimental ranges (Figs. 5(e) and 6(d)). A Ga content close to nominal value of 50% can only be achieved at either low laser energy (ca. 0.004 nJ with an effective pulse fraction < 5%) or the lowest voltage PF (ca. 20 %) within this work, where in both cases the sample experiences a high standing voltage. The result in pulsed laser mode is in agreement with previous reports on *c*-plane GaN samples prepared from epitaxial wafers (0.14 to 2.0 nJ) (Dawahre, et al., 2013), and from *c*-oriented GaN nanowires (0.003 nJ to 0.3 nJ) (Agrawal, et al., 2011). In both studies, a nitrogen content approaching the expected value was obtained only at the lowest laser energies studied. It should be noted that the detected Ga concentration appears non-uniform in the lateral directions (in approximate X/Y plane in the desorption map) in each run, apparently related to the crystallographic features such as poles and zone lines formed on the desorption maps. The observation is consistent with the analysis of nanowires (Diercks, et al., 2013).

The loss of nitrogen ions in the APT measurement, particularly for those analyses undertaken with increasingly high laser-pulse energies, remains an outstanding and poorly understood issue. It has previously been proposed that this erroneous measurement involves the generation of nitrogen neutrals which are not necessarily detectable by the experiment (Agrawal, et al., 2011; Dawahre, et al., 2013; Diercks, et al., 2013). It has been speculated that this may occur through the direct evaporation of neutral N_2 molecules from the surface of the specimen, which would fail to be detected by the experiment. However, this proposed mechanism still needs further investigation. Alternatively, it has also been proposed that N_2 neutrals can be formed by the dissociation of complex molecular ions post evaporation. Using a correlation analysis of detected ions, Saxey (Saxey, 2011) provided evidence indicating that the dissociation of larger complex ions. Specifically, it was shown that the dissociation of

GaN_3^{2+} ions into Ga^+, N^+ and N_2 species did play a role in the APT analysis of GaN. However, this study also demonstrated that this was not the primary mechanism for the compositional discrepancy, accounting for only a tiny fraction of the lost nitrogen.

A more straightforward explanation for this loss in compositional accuracy is that N and/or N_2 ions evaporate preferentially to Ga. At higher laser energies there is an increase in the evaporation of ions that are not correlated to the application of the laser pulse, as indicated by Fig. 5(d). It is feasible that relative to Ga a greater amount of N ions (or complex N ions) are erroneously identified as noise in the resulting mass spectrum, and hence a systematic decrease in the measure composition of nitrogen. However, it is unlikely that this alone could explain the observations in the low laser energy range (0.1 nJ and less) and in pulsed-voltage mode. Another possibility is driven by the frequency at which N_2 ions tend to evaporate as part of multi-ion events. This refers to situation where more than one ion is field evaporated by a single pulse. This can lead to a phenomenon known as pile-up (Gault, et al., 2012), which occurs when many ions of the same type arrive simultaneously at the detector. Pile-up results in the situation where this excess of information cannot be processed and leads to omission of these ions from the analysis. However, in view of the fact that measured Ga concentrations close to the theoretical stoichiometric ratio of GaN were obtained at a relative low laser pulse energy where a relative high fraction of multiple hits (e.g. about 20% in Fig. 5(c)) and a large ranged ion ratio in the mass spectrum (Fig. 5(d)) were involved, it is thus expected that the contribution of multiple hit events to deficient nitrogen measurement is not significant in this work. In addition, because the detected Ga composition close to the theoretical value of GaN was associated with a high standing voltage irrespective of whether pulsed laser or pulsed voltage mode was used, it is hypothesized that the underlying mechanism leading to the erroneously measured composition might be similar for both cases.

CONCLUSIONS

Discerning the extent of potential FIB implantation damage during specimen preparation is a significant concern for APT analysis for GaN-based materials. The application of monoisotopic Ga-69 during FIB specimen preparation enabled differentiation of implanted Ga from that naturally occurring in the specimen. Our analysis also demonstrated that significant amounts of Ga are unintentionally incorporated into the InAlN during sample growth.

The Ga implantation induced by FIB sample preparation was found within the reconstructed APT data when the sample was prepared with a relative high ‘clean-up’ voltage, for instance, in the first 10 nm of the analysis the implanted Ga content reached values as high as ~ 10 at.% in the case with at a 5 kV clean-up voltage. However it is shown here that this with appropriate precautions (Pt cap) and milling conditions (FIB clean-up voltages below 5 kV), damage can be dramatically reduced and certainly limited to depths of less than 20 nm. Hence, specimens should ideally be designed and fabricated such that any region-of-interest for analysis is at least this depth from the apex of the tip.

There exists a strong dependency of the measured Ga composition on the applied laser pulse energy. Measured composition were closest to the expected value for stoichiometry for the lowest laser-pulse energy applied - 0.004 nJ. For low-laser pulse energy a clear pole structure is seen in the desorption map, and surface migration of the atoms should therefore be minimised and hence spatial resolution optimised. Further, the relatively large ratio of ranged ion counts compared to all counts across the entire mass spectrum is indicative of the best signal-to-noise ratio. However, under these conditions there is also a relatively large fraction of multi-hit events (~ 22%).

A clear pole structure is also observed in the desorption map when the specimen is analysed under HV-pulsing conditions. However, under these conditions anomalous broad peaks are seen in the mass spectra. While increasing the pulse fraction did not affect the observed pole structure significantly, the contribution of the unexplained peaks ion to the mass spectrum degraded the quality of the analysis.

The results indicate that with appropriate FIB specimen preparation and experimental conditions APT provides a suitable approach to compositional analysis of nitride semiconductors, and validates many of the studies performed so far using this technique.

ACKNOWLEDGMENTS

FT would like to thank David A. Nicol for his kind help. The European Research Council has provided financial support under the European Community's Seventh Framework Programme (FP7/2007-2013)/ERC grant agreement no 279361 (MACONS).

REFERENCES

AGRAWAL, R., BERNAL, R.A., ISHEIM, D. & ESPINOSA, H.D. (2011). Characterizing atomic composition and dopant distribution in wide band gap semiconductor nanowires using laser-assisted atom probe tomography. J Phys Chem C **115**(36), 17688-17694.

AMBACHER, O. (1998). Growth and applications of Group III nitrides. J Phys D: Appl Phys **31**(20), 2653-2710.

Baloch, K.H., Johnston-Peck, A.C., Kisslinger, K., Stach, E.A. & Gradečak, S. (2013). Revisiting the "In-clustering" question in InGaN through the use of aberration-corrected electron microscopy below the knock-on threshold. Appl Phys Lett **102**(19), 191910.

Bennett, S. (2011). Nitride semiconductors studied by atom probe tomography and correlative techniques. University of Cambridge.

Bennett, S., Ulfig, R., Clifton, P., Kappers, M., Barnard, J., Humphreys, C. & Oliver, R. (2011). Atom probe tomography and transmission electron microscopy of a Mg-doped AlGaN/GaN superlattice. Ultramicroscopy **111**(3), 207-211.

Choi, S., Jin Kim, H., Lochner, Z., Kim, J., Dupuis, R.D., Fischer, A.M., Juday, R., Huang, Y., Li, T. & Huang, J.Y. (2014). Origins of unintentional incorporation of gallium in AlInN layers during epitaxial growth, part I: Growth of AlInN on AlN and effects of prior coating. J Cryst Growth **388**, 137-142.

Choi, S., Wu, F., Shivaraman, R., Young, E.C. & Speck, J.S. (2012). Observation of columnar microstructure in lattice-matched InAlN/GaN grown by plasma assisted molecular beam epitaxy. Appl Phys Lett **100**(23), 232102.

Cullen, D.A. & Smith, D.J. (2008). Assessment of surface damage and sidewall implantation in AlGaN-based high electron mobility transistor devices caused during focused-ion-beam milling. J Appl Phys **104**(9), 094304.

Datta, R., Kappers, M., Vickers, M., Barnard, J. & Humphreys, C. (2004). Growth and characterisation of GaN with reduced dislocation density. Superlattices Microstruct **36**(4), 393-401.

Dawahre, N., Shen, G., Renfrow, S.N., Kim, S.M. & Kung, P. (2013). Atom probe tomography of AlInN/GaN HEMT structures. J Vac Sci Technol, B **31**(4), 041802.

Devaraj, A., Colby, R., Hess, W.P., Perea, D.E. & Thevuthasan, S. (2013). Role of photoexcitation and field ionization in the measurement of accurate oxide stoichiometry by laser-assisted atom probe tomography. J Phys Chem Lett. **4**(6), 993-998.

Diercks, D.R., Gorman, B.P., Kirchhofer, R., Sanford, N., Bertness, K. & Brubaker, M. (2013). Atom probe tomography evaporation behavior of C-axis GaN nanowires: Crystallographic, stoichiometric, and detection efficiency aspects. J Appl Phys **114**(18), 184903.

Galtrey, M., Oliver, R., Kappers, M., McAleese, C., Zhu, D., Humphreys, C., Clifton, P., Larson, D. & Cerezo, A. (2008). Compositional inhomogeneity of a high-efficiency $In_xGa_{1-x}N$ based multiple quantum well ultraviolet emitter studied by three dimensional atom probe. Appl Phys Lett **92**(4), 041904.

Galtrey, M.J., Oliver, R.A., Kappers, M.J., Humphreys, C.J., Stokes, D.J., Clifton, P.H. & Cerezo, A. (2007). Three-dimensional atom probe studies of an $In_xGa_{1-x}N$ / GaN multiple quantum well structure: Assessment of possible indium clustering. Appl Phys Lett **90**(6), 061903.

Gault, B., Moody, M.P., Cairney, J.M. & Ringer, S.P. (2012). *Atom probe microscopy*. Springer.

Gault, B., Müller, M., La Fontaine, A., Moody, M., Shariq, A., Cerezo, A., Ringer, S. & Smith, G. (2010). Influence of surface migration on the spatial resolution of pulsed laser atom probe tomography. J Appl Phys **108**(4), 044904.

Götz, W., Kern, R., Chen, C., Liu, H., Steigerwald, D. & Fletcher, R. (1999). Hall-effect characterization of III–V nitride semiconductors for high efficiency light emitting diodes. Materials Science and Engineering: B **59**(1), 211-217.

Gu, G.H., Jang, D.H., Nam, K.B. & Park, C.G. (2013). Composition Fluctuation of In and Well-Width Fluctuation in InGaN/GaN Multiple Quantum Wells in Light-Emitting Diode Devices. Microsc Microanal **19**(S5), 99-104.

Ilegems, M. & Montgomery, H. (1973). Electrical properties of *n*-type vapor-grown gallium nitride. J Phys Chem Solids **34**(5), 885-895.

Jarjour, A.F., Taylor, R.A., Oliver, R.A., Kappers, M.J., Humphreys, C.J. & Tahraoui, A. (2007). Cavity-enhanced blue single-photon emission from a single InGaN/GaN quantum dot. Appl Phys Lett **91**(5), 052101.

Keller, S. & DenBaars, S.P. (2003). Metalorganic chemical vapor deposition of group III nitrides—a discussion of critical issues. J Cryst Growth **248**, 479-486.

Kellogg, G. & Tsong, T. (1980). Pulsed ‐ laser atom ‐ probe field ‐ ion microscopy. J Appl Phys **51**(2), 1184-1193.

Kelly, T.F., Vella, A., Bunton, J.H., Houard, J., Silaeva, E.P., Bogdanowicz, J. & Vandervorst, W. (2014). Laser pulsing of field evaporation in atom probe tomography. Curr Opin Solid State Mater Sci **18**(2), 81-89.

Kempshall, B., Schwarz, S., Prenitzer, B., Giannuzzi, L., Irwin, R. & Stevie, F. (2001). Ion channeling effects on the focused ion beam milling of Cu. J Vac Sci Technol, B **19**(3), 749-754.

Kim, J., Lochner, Z., Ji, M.-H., Choi, S., Kim, H.J., Kim, J.S., Dupuis, R.D., Fischer, A.M., Juday, R. & Huang, Y. (2014). Origins of unintentional incorporation of gallium in InAlN layers during epitaxial growth, part II: Effects of underlying layers and growth chamber conditions. J Cryst Growth **388**, 143-149.

Kirchhofer, R., Teague, M.C. & Gorman, B.P. (2013). Thermal effects on mass and spatial resolution during laser pulse atom probe tomography of cerium oxide. J Nucl Mater **436**(1), 23-28.

Larson, D., Foord, D., Petford-Long, A., Liew, H., Blamire, M., Cerezo, A. & Smith, G. (1999). Field-ion specimen preparation using focused ion-beam milling. Ultramicroscopy **79**(1), 287-293.

Mazumder, B., Kaun, S.W., Lu, J., Keller, S., Mishra, U.K. & Speck, J.S. (2013). Atom probe analysis of AlN interlayers in AlGaN/AlN/GaN heterostructures. Appl Phys Lett **102**(11), 111603.

Melmed, A., Martinka, M., Girvin, S., Sakurai, T. & Kuk, Y. (1981). Analysis of high resistivity semiconductor specimens in an energy ‐ compensated time ‐ of ‐ flight atom probe. Appl Phys Lett **39**(5), 416-417.

Miller, M.K., Cerezo, A., Hetherington, M. & Smith, G. (1996). Atom probe field ion microscopy.

Moy, C.K., Ranzi, G., Petersen, T.C. & Ringer, S.P. (2011). Macroscopic electrical field distribution and field-induced surface stresses of needle-shaped field emitters. Ultramicroscopy **111**(6), 397-404.

MÜLLER, E.W. & KRISHNASWAMY, S. (1974). Energy deficits in pulsed field evaporation and deficit compensated atom‐probe designs. Rev Sci Instrum **45**(9), 1053-1059.

MÜLLER, M., SMITH, G., GAULT, B. & GROVENOR, C. (2012). Phase separation in thick InGaN layers–A quantitative, nanoscale study by pulsed laser atom probe tomography. Acta Mater **60**(10), 4277-4285.

NAKAMURA, S., SENOH, M., IWASA, N. & NAGAHAMA, S.-I. (1995). High-brightness InGaN blue, green and yellow light-emitting diodes with quantum well structures. Jpn J Appl Phys, Part2 **34**, L797-L797.

OLIVER, R., BENNETT, S., ZHU, T., BEESLEY, D., KAPPERS, M., SAXEY, D., CEREZO, A. & HUMPHREYS, C. (2010). Microstructural origins of localization in InGaN quantum wells. J Phys D: Appl Phys **43**(35), 354003.

PROSA, T., CLIFTON, P., ZHONG, H., TYAGI, A., SHIVARAMAN, R., DENBAARS, S., NAKAMURA, S. & SPECK, J. (2011). Atom probe analysis of interfacial abruptness and clustering within a single $In_xGa_{1-x}N$ quantum well device on semipolar (10 1 1) GaN substrate. Appl Phys Lett **98**(19), 191903.

PROSA, T., OLSON, D., GEISER, B., LARSON, D., HENRY, K. & STEEL, E. (2013). Analysis of implanted silicon dopant profiles. Ultramicroscopy **132**, 179-185.

RHODE, S., HORTON, M., KAPPERS, M., ZHANG, S., HUMPHREYS, C., DUSANE, R., SAHONTA, S.-L. & MORAM, M. (2013). Mg Doping Affects Dislocation Core Structures in GaN. Phys Rev Lett **111**(2), 025502.

RILEY, J.R., BERNAL, R.A., LI, Q., ESPINOSA, H.D., WANG, G.T. & LAUHON, L.J. (2012). Atom probe tomography of a-axis GaN nanowires: analysis of nonstoichiometric evaporation behavior. ACS nano **6**(5), 3898-3906.

RILEY, J.R., DETCHPROHM, T., WETZEL, C. & LAUHON, L.J. (2014). On the reliable analysis of indium mole fraction within $In_xGa_{1-x}N$ quantum wells using atom probe tomography. Appl Phys Lett **104**(15), 152102.

SADLER, T.C., KAPPERS, M.J. & OLIVER, R.A. (2011). The effects of varying metal precursor fluxes on the growth of InAlN by metal organic vapour phase epitaxy. J Cryst Growth **314**(1), 13-20.

Sanford, N., Blanchard, P., Brubaker, M., Bertness, K., Roshko, A., Schlager, J., Kirchhofer, R., Diercks, D. & Gorman, B. (2014). Laser‐assisted atom probe tomography of MBE grown GaN nanowire heterostructures. physica status solidi (c) **11**(3‐4), 608-612.

Saxey, D. (2011). Correlated ion analysis and the interpretation of atom probe mass spectra. Ultramicroscopy **111**(6), 473-479.

Silaeva, E.P., Karahka, M. & Kreuzer, H. (2013). Atom Probe Tomography and field evaporation of insulators and semiconductors: Theoretical issues. Curr Opin Solid State Mater Sci **17**(5), 211-216.

Smeeton, T., Kappers, M., Barnard, J., Vickers, M. & Humphreys, C. (2003). Electron-beam-induced strain within InGaN quantum wells: False indium “cluster” detection in the transmission electron microscope. Appl Phys Lett **83**(26), 5419-5421.

Smith, M.D., Taylor, E., Sadler, T.C., Zubialevich, V.Z., Lorenz, K., Li, H.N., O'Connell, J., Alves, E., Holmes, J. & Martin, R. (2014). Determination of Ga auto-incorporation in nominal InAlN epilayers grown by MOCVD. J Mater Chem C.

Speck, J. & Chichibu, S. (2009). Nonpolar and semipolar group III nitride-based materials. MRS Bull **34**(05), 304-312.

Stepień, Z.M. & Tsong, T.T. (1998). Formation of metal hydride ions in low-temperature field evaporation. Surf Sci **409**(1), 57-68.

Tamura, H., Tsukada, M., McKenna, K., Shluger, A., Ohkubo, T. & Hono, K. (2012). Laser-assisted field evaporation from insulators triggered by photoinduced hole accumulation. Physical Review B **86**(19), 195430.

Tang, F., Gault, B., Ringer, S.P. & Cairney, J.M. (2010). Optimization of pulsed laser atom probe (PLAP) for the analysis of nanocomposite Ti–Si–N films. Ultramicroscopy **110**(7), 836-843.

Tang, F., Gianola, D., Moody, M., Hemker, K. & Cairney, J. (2012). Observations of grain boundary impurities in nanocrystalline Al and their influence on microstructural stability and mechanical behaviour. Acta Mater **60**(3), 1038-1047.

Tang, F., Zhu, T., Oehler, F., Fu, W.Y., Griffiths, J.T., Massabuau, F.C.-P., Kappers, M.J., Martin, T.L., Bagot, P.A. & Moody, M.P. (2015). Indium clustering in a-plane InGaN quantum wells as evidenced by atom probe tomography. Appl Phys Lett **106**(7), 072104.

Thompson, K., Gorman, B., Larson, D., van Leer, B. & Hong, L. (2006). Minimization of Ga induced FIB damage using low energy clean-up. Microsc Microanal **12**(S02), 1736-1737.

Thompson, K., Lawrence, D., Larson, D., Olson, J., Kelly, T. & Gorman, B. (2007). In situ site-specific specimen preparation for atom probe tomography. Ultramicroscopy **107**(2), 131-139.

Tsong, T. (1984). Formation of multiatomic cluster ions of silicon in pulsed ‐ laser stimulated field desorption. Appl Phys Lett **45**(10), 1149-1151.

Yao, L., Gault, B., Cairney, J. & Ringer, S. (2010). On the multiplicity of field evaporation events in atom probe: a new dimension to the analysis of mass spectra. Philos Mag Lett **90**(2), 121-129.

Zhu, D., Wallis, D. & Humphreys, C. (2013). Prospects of III-nitride optoelectronics grown on Si. Rep Prog Phys **76**(10), 106501.

Zhu, J., Fan, Y., Zhang, H., Lu, G., Wang, H., Zhao, D., Jiang, D., Liu, Z., Zhang, S. & Chen, G. (2012). Contribution of GaN template to the unexpected Ga atoms incorporated into AlInN epilayers grown under an indium-very-rich condition by metalorganic chemical vapor deposition (MOCVD). J Cryst Growth **348**(1), 25-30.

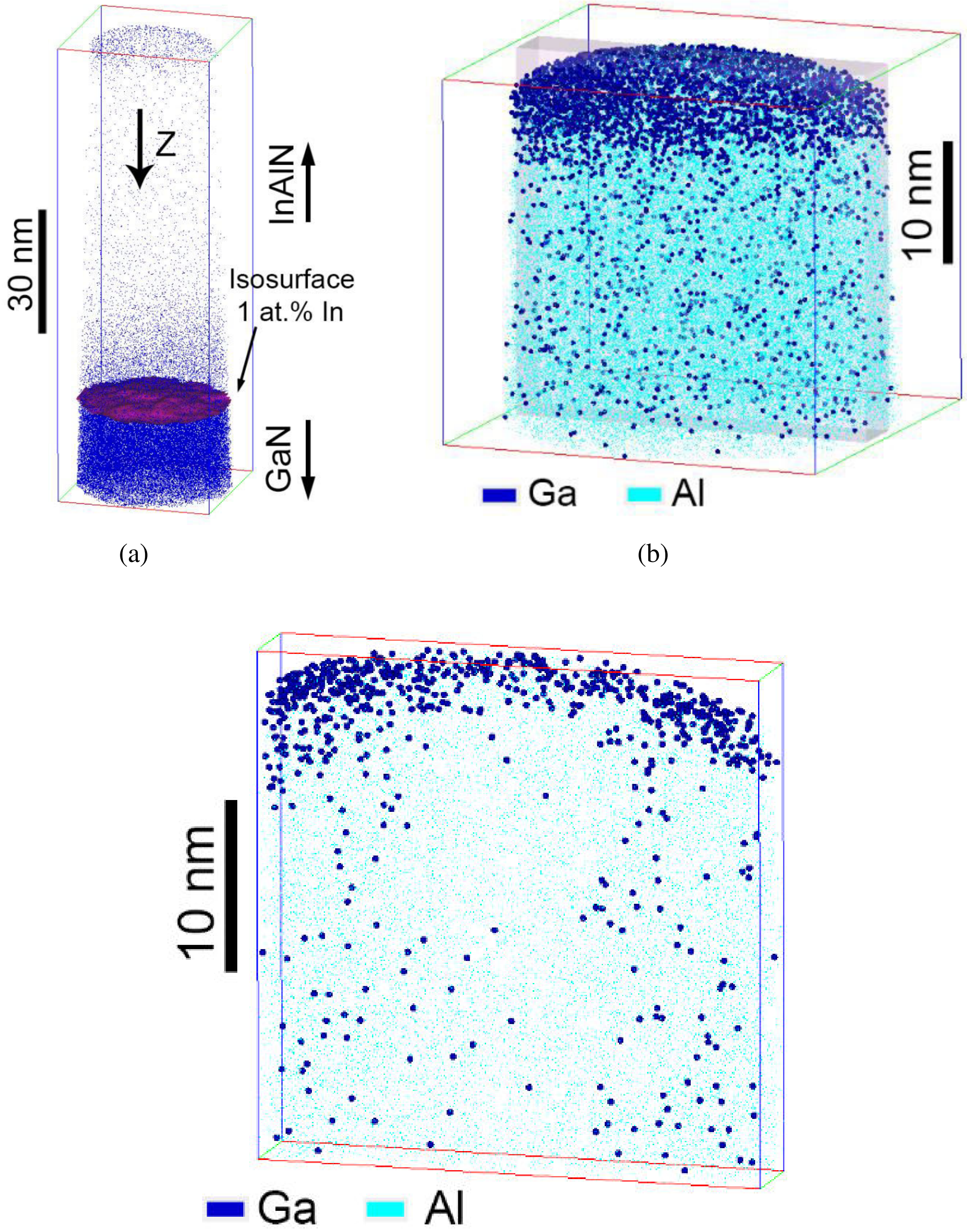

(a) (b)

(c)

Figure 1. Ga distributions in a tip with a ‘clean-up’ FIB voltage of 5 kV. (a) 3D reconstruction showing 20% of the reconstructed Ga atoms, (b) 3D reconstruction from the top of (a) displaying 50% of the detected Ga atoms and 50% of the detected Al atoms and (c) of a 5 nm slice whose position is designated in (b).

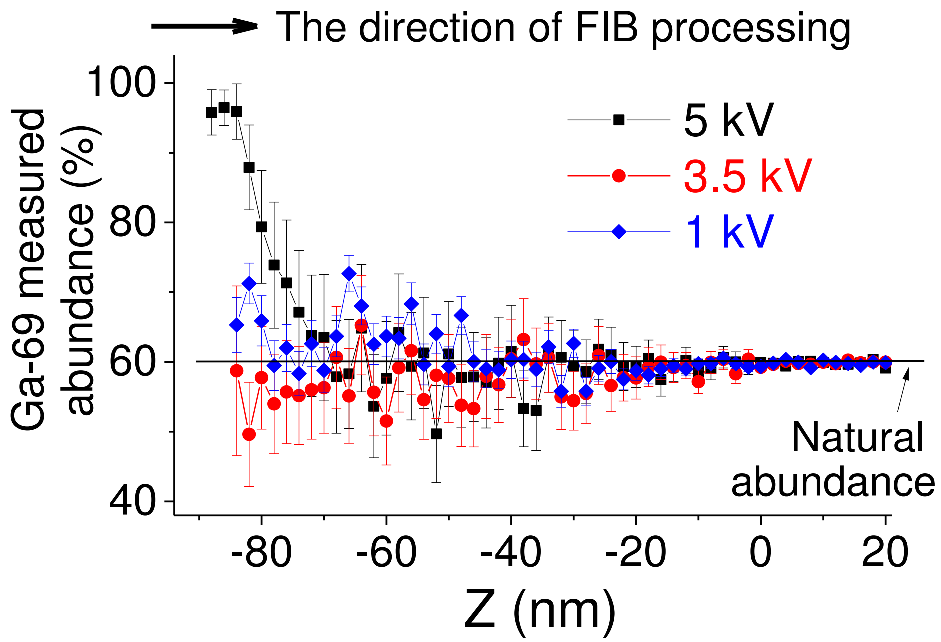

(a)

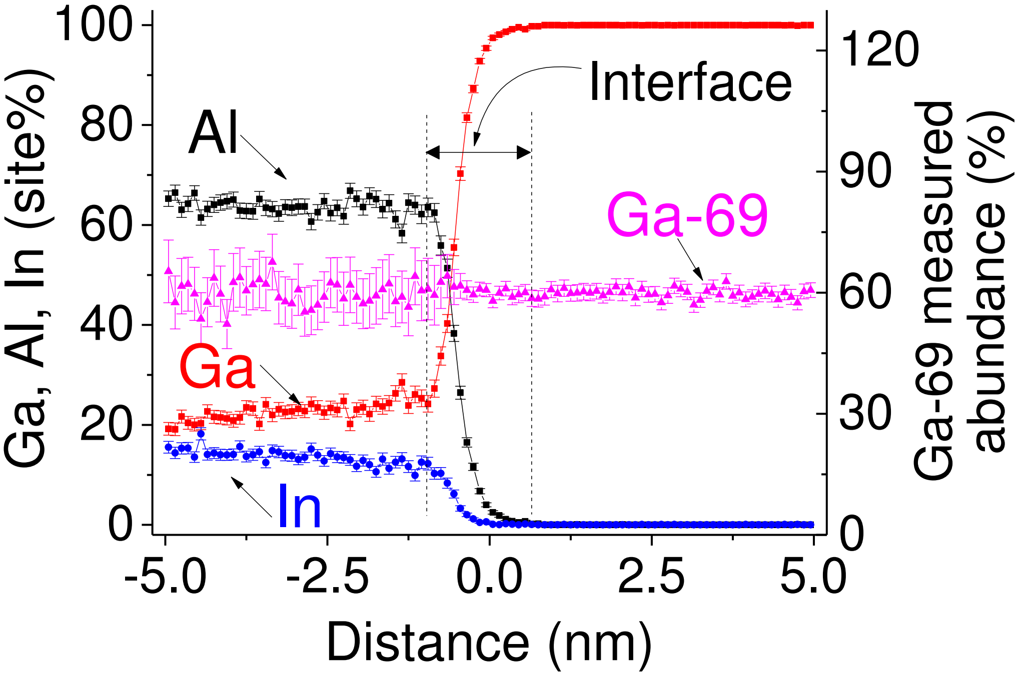

(b)

Figure 2. The summary of 1D concentration profiles of (a) Ga-69 measured abundance along the z-axis (as designated in Fig. 1(a)) in three samples with variable ‘clean-up’ FIB voltages, in which the coordinates are aligned against the InAlN/GaN interface; and (b) the proxigram computed using 1 at.% In isosurfaces on the case with a 5 kV ‘clean up’ voltage, where a sharp interface across the InAlN/GaN heterostructure is revealed but no apparent FIB-implanted Ga as manifested by the Ga-69 profile.

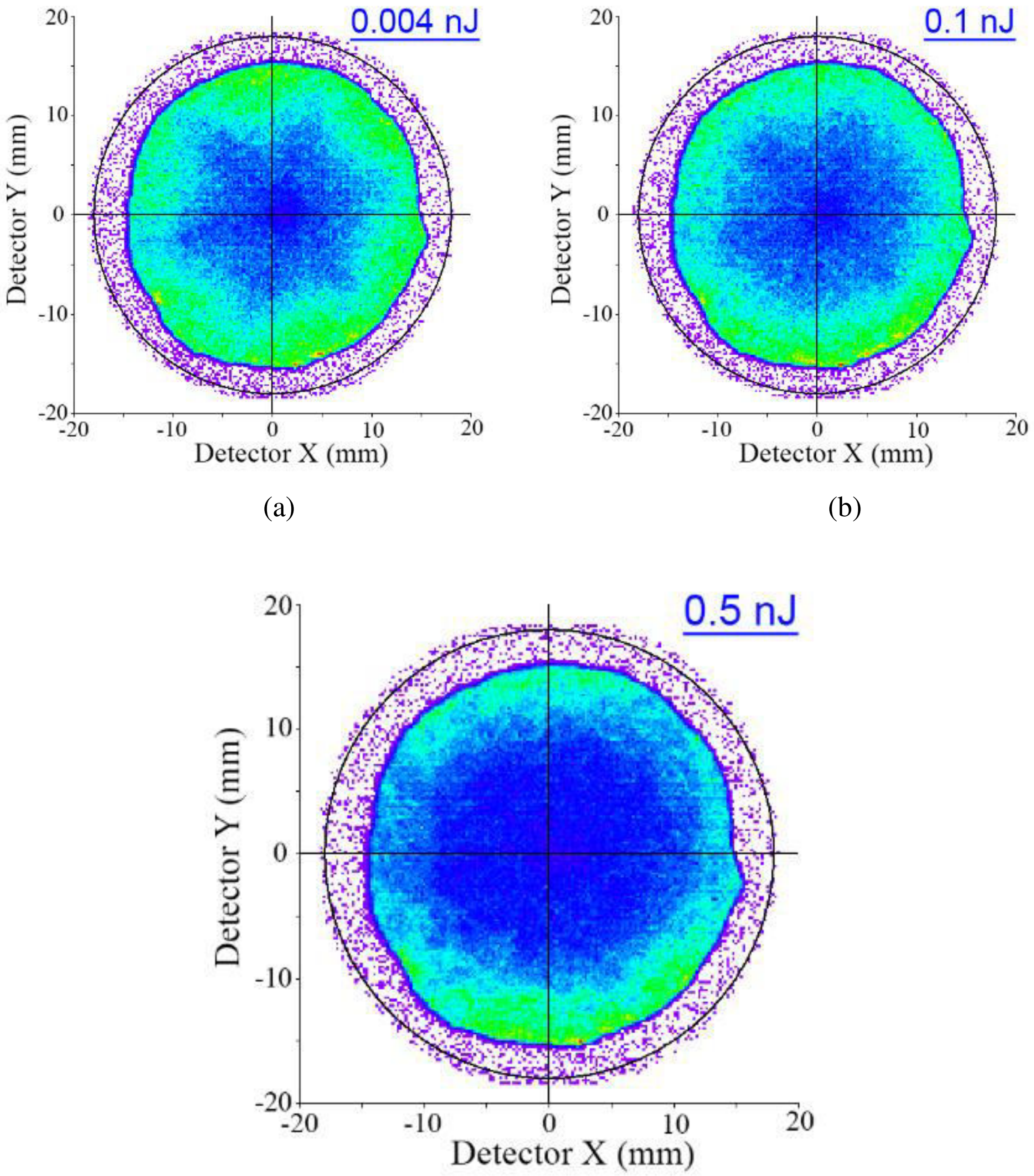

(a) (b)

(c)

Figure 3. Evolution of desorption map with increasing laser energy from the analysis of the underlying GaN layer. Each data set is about 10^6 hits. The crystallographic pole structures in the case at 0.004 nJ clearly reveals a 6-fold symmetry, indicative of {0001} projection.

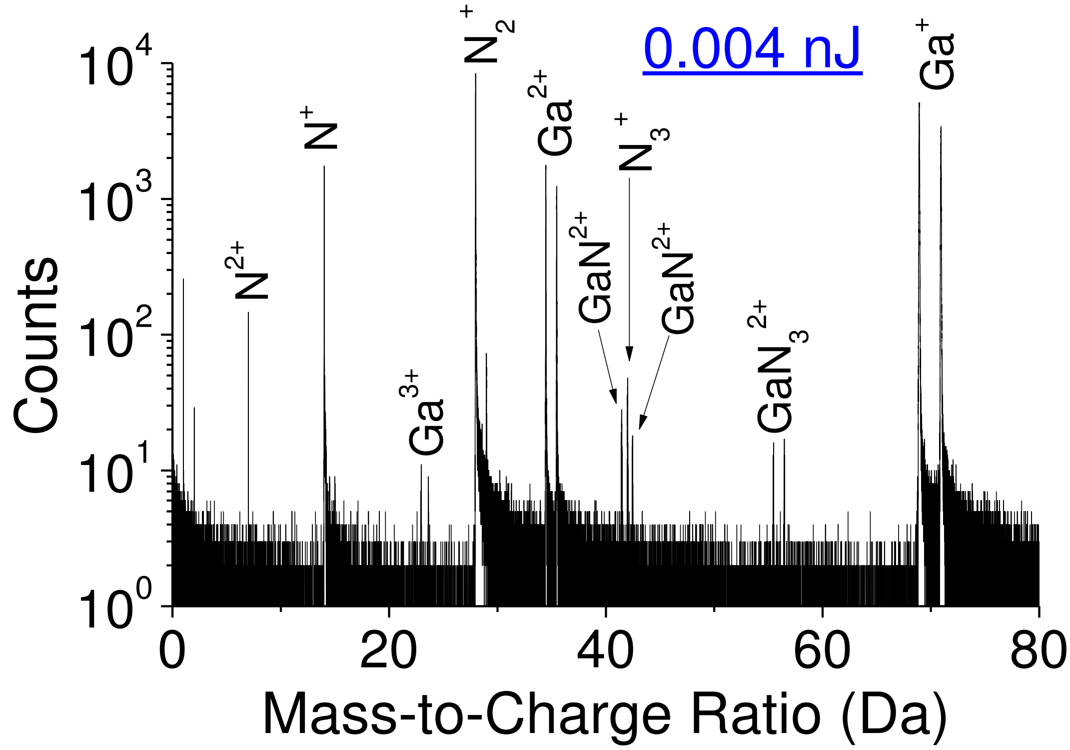
0.004 nJ
N^+_2
Ga^+
N^+
Ga^{2+}
N_3^+
N^{2+}
GaN^{2+}
GaN^{2+}
Ga^{3+}
GaN_3^{2+}
Counts
10^4
10^3
10^2
10^1
10^0
0
20
40
60
80
Mass-to-Charge Ratio (Da)

(a)

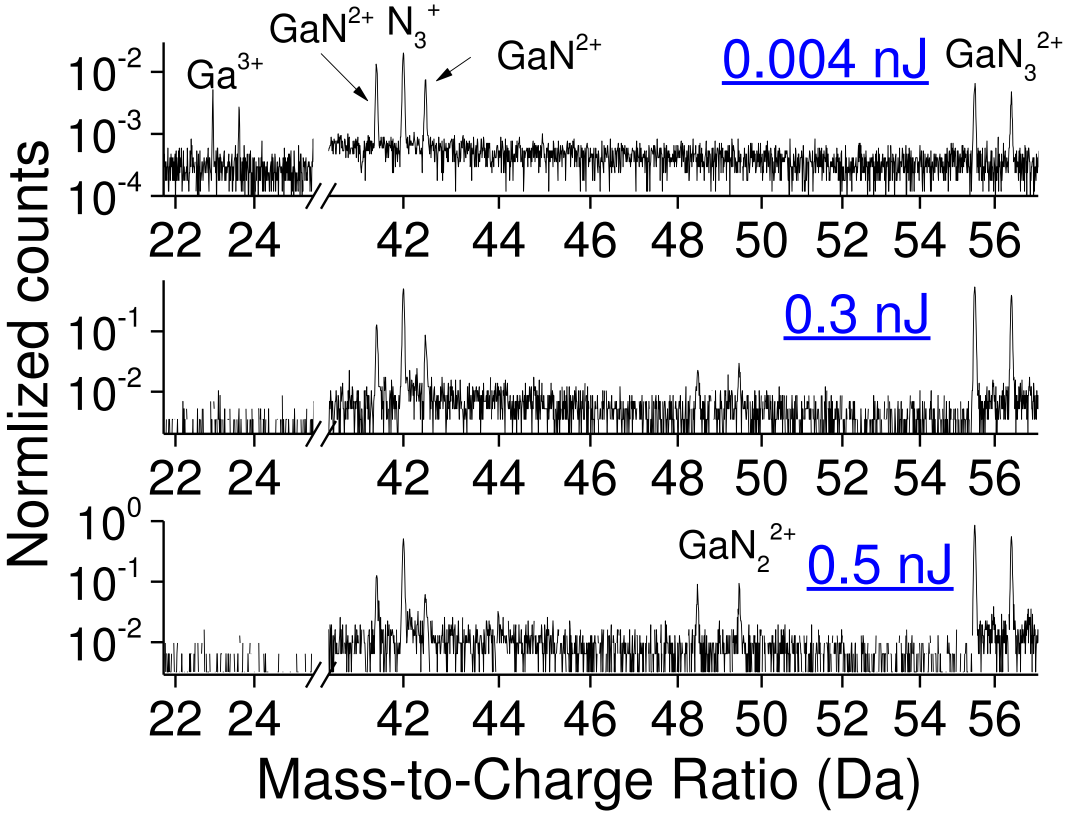
GaN^{2+}
N_3^+
Ga^{3+}
GaN^{2+}
0.004 nJ
GaN_3^{2+}
0.3 nJ
0.5 nJ
GaN_2^{2+}
Normlized counts
10^{-2}
10^{-3}
10^{-4}
10^{-1}
10^{-2}
10^0
10^{-1}
10^{-2}
22
24
42
44
46
48
50
52
54
56
Mass-to-Charge Ratio (Da)

(b)

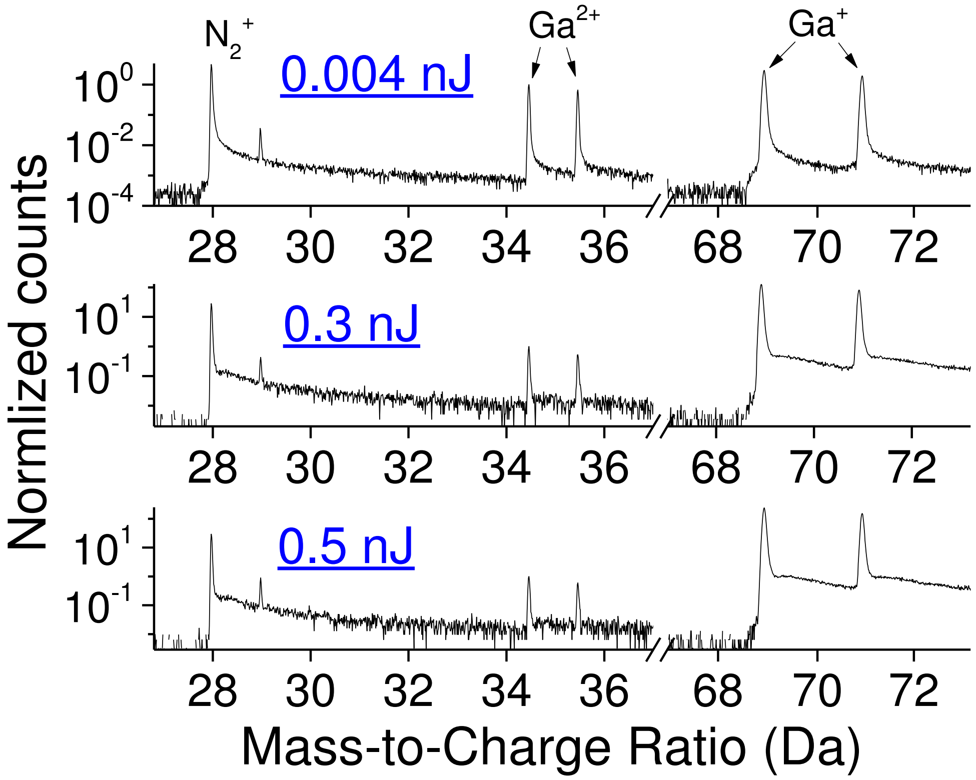

(c)

Figure 4. (a) Overview of mass spectrum obtained at the 0.004 nJ pulse laser energy, and the evolution of Ga^{3+}, GaN^{2+}, GaN_2^{2+} and GaN_3^{2+} ions (b) and N_2^+, Ga^{2+} and Ga^+ ions (c) as a function of laser energy. In (b) and (c), each mass spectrum was normalized relative to the peak of Ga^{2+} ions.

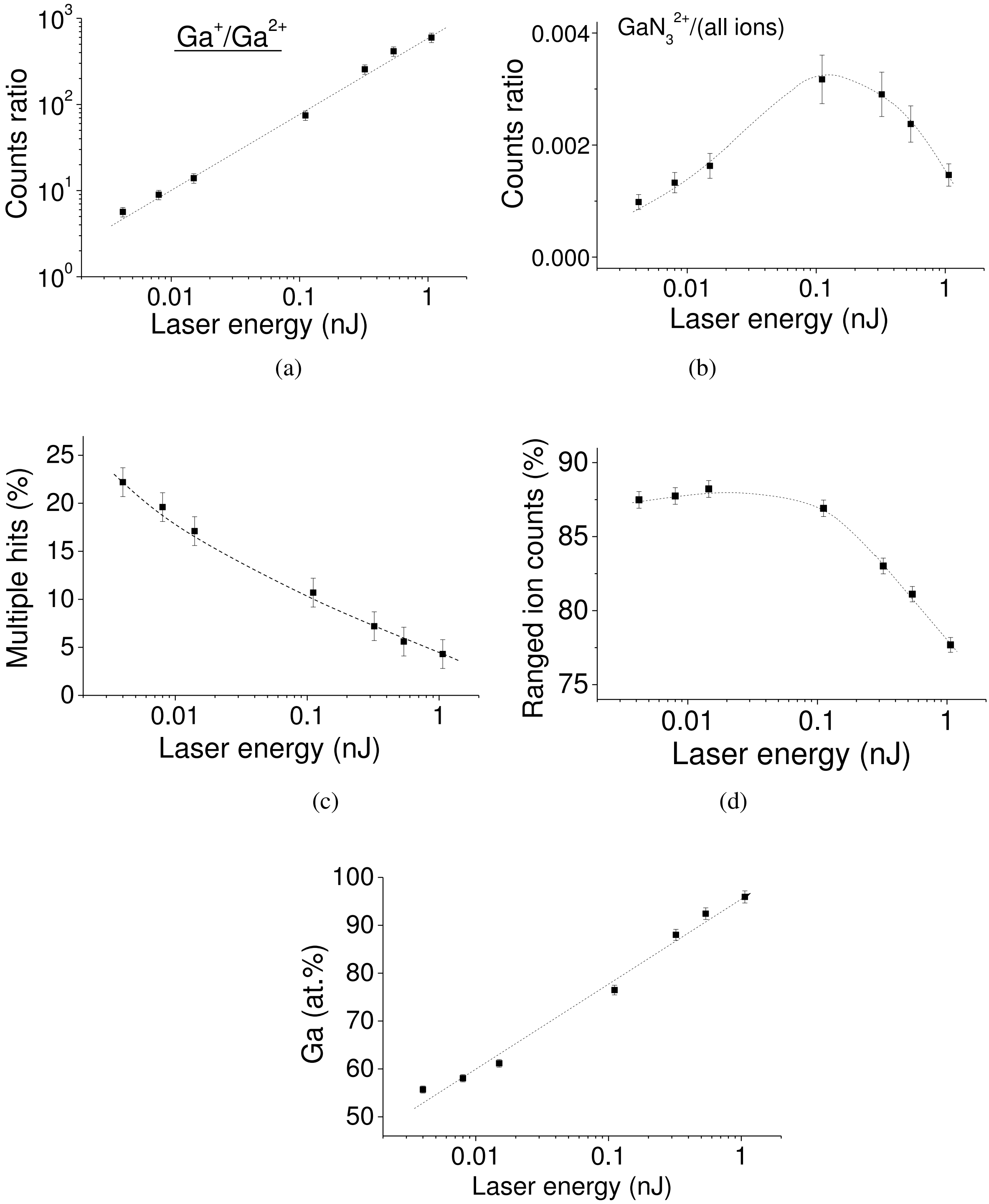

(a) (b)

(c) (d)

(e)

Figure 5. The impact of laser energy on (a) the charge-state-ratio of Ga$^+$/Ga^{2+} ions, (b) the ratio of GaN$_3^{2+}$/(all ions), (c) the percent of multiple hit events, (d) the ratio of ranged ion counts over that entire mass spectrum and (e) the detected Ga concentration. The curves are drawn as guides to the eye.

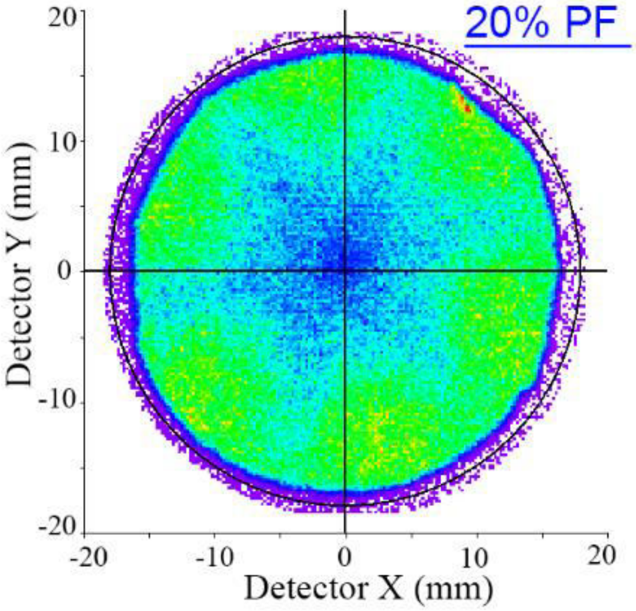
20% PF
Detector Y (mm)
Detector X (mm)
20
10
0
-10
-20
-20
-10
0
10
20

(a)

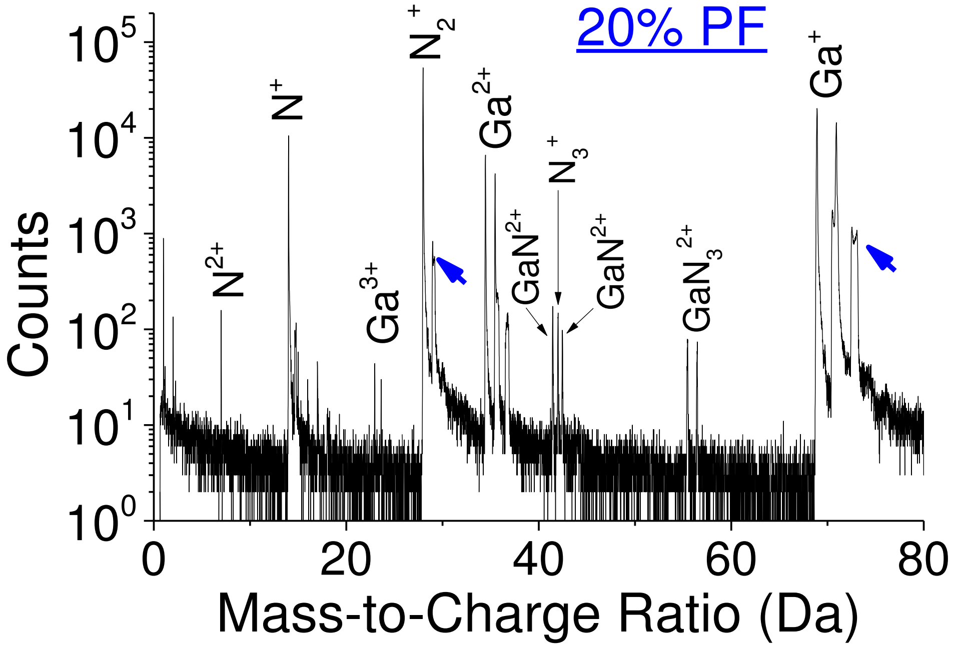
20% PF
Counts
Mass-to-Charge Ratio (Da)
10^5
10^4
10^3
10^2
10^1
10^0
0
20
40
60
80
N^{2+}
N^+
Ga^{3+}
N_2^+
Ga^{2+}
GaN^{2+}
N_3^+
GaN^{2+}
GaN_3^{2+}
Ga^+

(b)

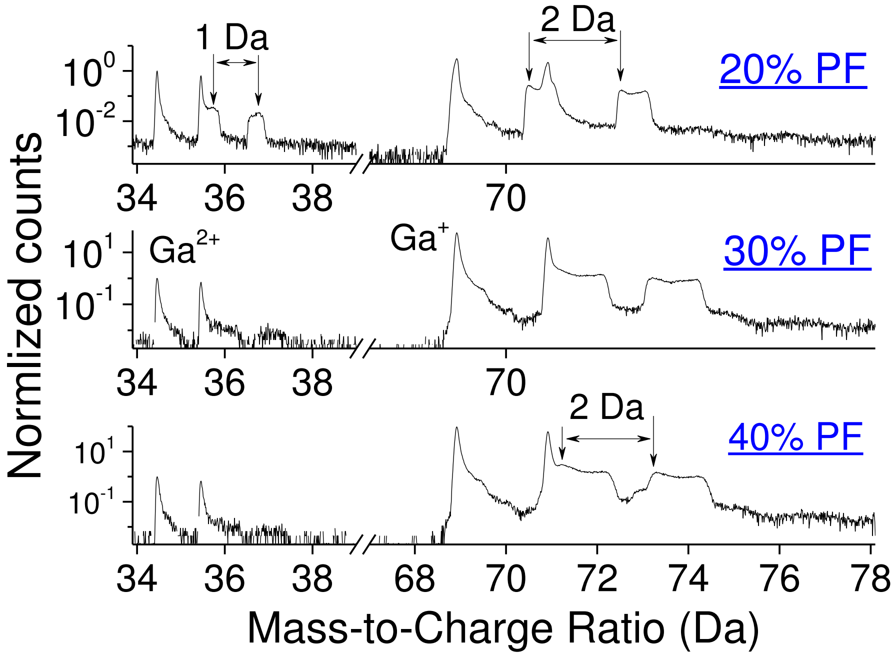

(c)

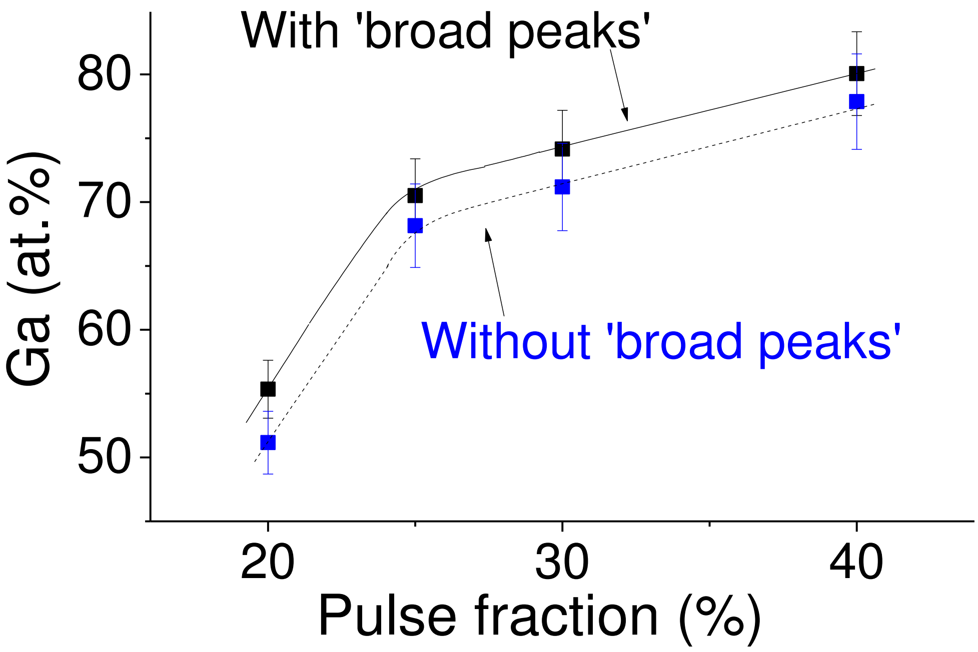

(d)

Figure 6. (a) A desorption map of GaN buffer layer collected at the voltage-pulse mode with a 20% pulse fraction and (b) its corresponding mass spectrum, (c) the evolutions of Ga$^+$ and Ga^{2+} peaks and anomalous peaks, where the mass spectrum was normalized with respect to the counts of Ga^{2+} ions, and (d) Ga concentration as a function of pulse fraction, where the line is simply drawn to guide the eye.